1 **Paleoearthquake reconstruction on an impure limestone fault scarp at Sparta, Greece**

3 Bradley W. Goodfellow[1,2,3,4], Marc W. Caffee[5,6], Greg Chmiel[5], Ruben Fritzon[1,3#], Alasdair

4 Skelton[2,3], Arjen P. Stroeven[1,3*]

6 [1]Geomorphology and Glaciology, Department of Physical Geography, Stockholm University, Stockholm,

7 Sweden

8 [2]Department of Geological Sciences, Stockholm University, Stockholm, Sweden

9 [3]Bolin Centre for Climate Research, Stockholm University, Stockholm, Sweden

10 [4]Geological Survey of Sweden, Killiansgatan 10, Lund, Sweden

11 [5]Department of Physics and Astronomy/Purdue Rare Isotope Measurement Laboratory,

12 Purdue University, West Lafayette, USA

13 [6]Department of Earth, Atmospheric, and Planetary Sciences, Purdue University, West

14 Lafayette, USA

16 *Corresponding author

17 Email: arjen.stroeven@natgeo.su.se

18 Phone: +46(0)8-16 4230

19 #Now at Celsiusskolan, Sporthallsvägen 7, 828 33 Edsbyn, Sweden

22 **Abstract**

24 Reliable reconstructions of paleoseismicity are useful for understanding, and mitigating,

25 seismic hazard risks. In this study, we apply cosmogenic ^{36}Cl exposure-age dating and

26 concentrations of rare-earth elements and yttrium (REY) to unravelling the paleoseismic

27 history of the Sparta fault, Greece, which is a range-bounding normal fault developed in

28 limestone. Modeling of ^{36}Cl concentrations along two vertical profiles on the Sparta Fault

29 indicates a clustering of four earthquakes within a 1.5 kyr period that culminated with the 464

30 B.C.E. event that devastated Spartan society. Cumulative uplift was as high as 2.8 mm yr^{-1}

31 during that period, compared with ~0.6–0.9 mm a-1 over the preceding 2.7–4.4 kyr. Because

32 earthquake activity may shift between faults in extensional settings, a large magnitude

33 earthquake is not necessarily indicated as being overdue by the present ~2.5 kyr quiescent

34 period. More generally, accurate identification of individual earthquakes is presently

35 constrained by spatial variations in ^{36}Cl concentration profiles that reflect neither exposure

36 duration nor imprints of former soil profiles. In cases where this is attributable to

37   mineralogical variations, such as in the Sparta fault scarp, present chemical preparation

38   techniques for AMS measurement of ^{36}Cl may insufficiently account for those variations.

40   The Sparta fault scarp is composed of fault breccia, which contains quartz and clay-lined

41   pores, in addition to host rock-derived clasts of calcite and microcrystalline calcite cement.

42   The exchange of REY between the hanging wall colluvium and the fault scarp calcite, which

43   has been applied to the study of paleoseismicity on other limestone normal faults, is

44   overwhelmed on this fault scarp by REY attached to the breccia pore clays. Holocene

45   earthquakes and their magnitudes, inferred from fault slip lengths, therefore cannot be

46   inferred from REY data for impure limestone faults such as the Sparta fault but, rather, these

47   data may indicate processes of fault evolution in the Earth's near surface.

48

49

50   **Keywords**

51   ^{36}Cl exposure dating; earthquake; limestone; normal fault; REY elements; Sparta fault

52

53   **1 Introduction**

54

55   Seismic hazard risks are significant in many parts of the world and studying the magnitude,

56   recurrence, mechanisms, and impacts of past earthquakes helps form a basis for mitigating

57   current and future risk. While historical earthquake records are a crucial archive (Gürpinar,

58   2005), their spatial distribution is patchy and the recurrence interval of large earthquakes on

59   many faults exceeds historical record lengths. Paleoseismic studies that use geologic evidence

60   to infer past earthquakes, and even potentially unravel key earthquake characteristics, such as

61   timing, recurrence intervals, and the magnitudes of slip and shaking intensity, are therefore an

62 essential component of seismic hazard risk mitigation (McCalpin, 2009, p. 24). Topographic

63 expressions of tectonic faults, the displacement of surficial sediments revealed in trenches,

64 and geochemical alterations on subaerially exposed fault surfaces, may each provide evidence

65 useful to the study of paleoseismicity (e.g., Benedetti et al., 2002; Dramis and Blumetti,

66 2005; Michetti et al., 2005; Carcaillet et al., 2008; Manighetti et al., 2010; Mouslopoulou et

67 al., 2011; Smith et al., 2014; Cowie et al., 2017; Mozafari et al., 2022). In this study we use

68 cosmogenic ^{36}Cl and concentrations of rare-earth elements and yttrium (REY) to study the

69 paleoseismic history of the Sparta fault at Anogia, Greece (Fig. 1a, b).

70

71 The Mediterranean is a densely populated seismically active region that was subjected to

72 7360 earthquakes of magnitude *(M)* > 4 during 1998–2010 (Godey et al., 2013). Within the

73 Aegean tectonic plate (Fig. 1a), and around its margins, there were >1450 such earthquakes

74 during this period, 77 of which were M > 5. In central Greece, earthquakes are associated

75 with normal faults, which occur because of extension of the Aegean plate (Jolivet et al.,

76 2013). In limestone, they may be identified by spectacular scarps, which form from the

77 accumulation of bedrock slip that occurs during successive earthquakes. Holocene fault

78 scarps can be well-preserved (Armijo et al., 1991), which makes them potentially suitable

79 targets for paleoseismic studies.

80

81 Earthquakes inferred from incremental slips of limestone normal faults have been dated with

82 concentrations of *in situ*-produced cosmogenic ^{36}Cl (Zreda and Noller, 1998; Mitchell et al.,

83 2001; Benedetti et al., 2002; Palumbo et al., 2004; Schlagenhauf et al., 2010; Tesson et al.,

84 2016; Cowie et al., 2017; Mozafari et al., 2022). This nuclide is produced from spallogenic

85 and muonic reactions that occur in ^{40}Ca when limestone is exposed to cosmogenic radiation.

86 Following an earthquake, the newly exposed scarp segment accumulates ^{36}Cl, the

87   concentration of which is dependent upon the duration of subaerial exposure, thereby

88   potentially allowing the earthquake to be dated. More recently, ^{36}Cl dating has been

89   complemented with measurements of REY because their distribution vertically along fault

90   scarps may indicate imprints of former hanging-wall soil REY that have been uplifted by

91   successive earthquakes (Carcaillet et al., 2008; Manighetti et al., 2010; Mouslopoulou et al.,

92   2011; Moraetis et al., 2015). Peaks in REY may represent former soil surfaces and their

93   spacing may permit paleoseismic inferences such as the number of slip events, vertical

94   displacement lengths, and earthquake magnitudes. These inferences can be made

95   independently of ^{36}Cl measurements, which can help to verify and strengthen interpretations

96   of past earthquakes using this nuclide.

97

98   A pioneering cosmogenic ^{36}Cl study of the Sparta fault by Benedetti et al. (2002) guided our

99   interest because they found evidence at Parori (Fig. 1b) for the historically recorded 464

100   B.C.E. earthquake that destroyed Sparta (Armijo et al., 1991), and inferred an additional five

101   older earthquakes. However, they were unable to date the historical slip at nearby Anogia.

102   Our study objectives were to: (i) Re-date the paleoseismicity of the Sparta fault at Anogia, to

103   test for the surprising absence of the 464 B.C.E. earthquake, by taking advantage of recent

104   advances in both the measurement of ^{36}Cl and earthquake modelling that accounts for all ^{36}Cl

105   production pathways and shielding effects (Schlagenhauf et al., 2010), and; (ii) Complement

106   the ^{36}Cl dating with measurement of REY to best constrain the paleoseismic history of this

107   fault.

108

109   **2 Geological Setting**

110

111   The Sparta fault is a 64 km long, NNW–SSE striking, range-bounding normal fault in

112   southern Peloponnese (Fig. 1a, b). It separates the eastern flank of the Taygetos Mountains

113   (maximum elevation of 2407 m a.s.l.) from the Sparta Basin (Fig. 1b). The Sparta fault is part

114   of a larger normal fault system, which exceeds 150 km in length, and is matched on the

115   western margin of the Taygetos Mountains by the antithetical Kalamata fault and other

116   similar faults located offshore of the Mani Peninsula (Fig. 1a; Armijo et al., 1991). The

117   subaerially exposed scarp of the Sparta fault is developed in late Senonian-Eocene limestones

118   of the Ionian unit (Institute for Geology and Subsurface Research, 1969; Armijo et al., 1991).

119   Folded and tilted Permian to early Triassic pelitic and psammitic sedimentary and

120   metasedimentary units outcrop in the Taygetos Mountains and are also offset by the Sparta

121   fault at depth (Institute for Geology and Subsurface Research, 1969; Armijo et al., 1991).

122   Geomorphic evidence for Quaternary uplift along the eastern flank of the Taygetos

123   Mountains includes steep triangular facets (20°–40°) that are hundreds of meters high along

124   the central portion of the range and decrease in height towards the N and S, wineglass

125   canyons, perched valleys, and alluvial fans having up to 4 m of entrenchment near the Sparta

126   fault trace (Armijo et al., 1991; Benedetti et al., 2002; Pope and Wilkinson, 2005;

127   Papanikolaou et al., 2013). Collectively, the evidence indicates a tectonically active

128   environment.

129

130   The Sparta fault scarp is nearly continuous along strike and it reaches a maximum height of

131   10–12 m in its central portion but tapers towards both ends. Hanging wall erosion associated

132   with stream incision can locally form higher scarp segments. The scarp has a 65°–68° dip

133   and, in all but a few locations, slickensides have been eroded away following exhumation.

134   The slope of the hanging wall ground surface matches that upslope of the footwall, which

135   indicates a contiguous hillslope prior to formation of the present scarp and that sediment

136   accumulation at the scarp base is generally minor. However, wedges of sediment are locally

137   present on the hanging wall and in some places are welded to the scarp face, in positions now

138   perched above the hanging wall (Fig. S1). These wedges may have been perched by

139   earthquake-induced displacement on the Sparta fault or are debris deposits from mass

140   movements that have partly eroded. It is possible that other sediment wedges were also

141   formerly attached to the scarp face but have since fallen off.

142

143   Our sampling site is located at Anogia, where the Sparta fault scarp is 6.8 m high (Fig. 1c),

144   sparsely fractured, and displays a smooth surface texture (Fig. 1d-e). Slickenside traces are

145   visible, and the surface displays a black coating, like those commonly occurring on limestone

146   and which contain higher concentrations of SiO_2 and Al_2O_3 than the underlying rock

147   (Carcaillet et al., 2008). The scarp surface at Anogia also displays a spatially variable

148   distribution of subaerial weathering features such as rills and dissolution pits, which we

149   avoided in our sampling. The lower-angle hillslopes on both the foot wall (above the fault

150   scarp) and hanging wall display a patchy distribution of frequent bedrock outcrops and an

151   indurated allochthonous regolith composed of limestone clasts, with a matrix of red aeolian

152   dust and calcite cement. An outcrop of limestone about 50 m upslope of the fault scarp

153   reveals folded and tilted bedding. The bedding nearest to the scarp has a dip of 45–60° and a

154   strike of 268–279°, which corresponds with those for the fault scarp, indicating that faulting

155   appears to exploit these structural weaknesses in the bedrock.

156

157

158   **3 Methods**

159

160 To study the paleoseismicity of the Sparta fault, we combined Accelerated Mass

161 Spectrometry (AMS) measurements of cosmogenic ^{36}Cl concentrations from samples

162 collected from the Sparta fault scarp with field and laboratory analyses of scarp composition

163 and mineralogy, and with field measurements of hanging wall soil composition and pH. We

164 made these measurements by sampling a vertical ^{36}Cl profile at Anogia, upwards from the

165 ground surface and adjacent to the sampling transect of Benedetti et al. (2002) for direct

166 comparison with that pre-existing record (Fig. 1c). We also took samples for ^{36}Cl and

167 mineralogical analyses, including REY, from a second vertical profile located about 50 m to

168 the south (Fig. 1c). We chose this additional site for its smooth, non-fractured, fault scarp

169 surface, and sampling was completed from the top of the scarp to 80 cm below the present

170 ground surface, following hand excavation of a pit.

171

3.1 ^{36}Cl concentrations

173 We sampled the first profile, adjacent to the southern margin of the Benedetti et al. (2002)

174 profile, for ^{36}Cl by using an angle grinder to cut 10*20*2.5 cm (*h*w*d*) slabs from the

175 ground surface to a height of 3.9 m (Fig. 1c, d). Because of a crack in the fault scarp at 1.1 m

176 above the ground, the transect was shifted sideways (towards the north) by 40 cm, thus

177 duplicating the measurement at 1.1 m. A total of 37 samples from this profile were measured

178 for ^{36}Cl concentration. We sampled the second profile, ~ 50 m further to the south, for ^{36}Cl

179 and mineralogical analyses initially by drilling 14 cores of 4 cm diameter to a depth of 3 cm

180 into the scarp surface (Fig. 1c, e). Four of these cores were spaced at 20 cm intervals below

181 the ground surface and eight were spaced at 80 cm intervals above the ground surface to a

182 height of 6.4 m, which is 0.4 m below the top of the scarp. These samples were augmented by

183 another two drill core samples at 1.2 m and at 6.0 m. Subsequently, we took 20 samples from

184 this profile using an angle grinder to cut 10*20*2.5 cm (*h*w*d*) slabs from the ground

185   surface to a height of 2.0 m (Fig. 1c). A total of 71 samples from the three profiles were

186   subjected to preparation chemistry for ^{36}Cl targets and measured using AMS.

187

188   For ^{36}Cl measurements, limestone samples were crushed to approximately 0.5 mm diameter

189   and the whole sample was used without removing any size fraction through sieving. Prior to

190   partial dissolution approximately 120 g of crushed material was washed with deionized water

191   to remove fines. Following Stone et al. (1996), meteoric ^{36}Cl was removed using two cycles

192   of partial dissolution with nitric acid to dissolve 5% (by mass) of the carbonate each time. To

193   prepare the AMS target we used 30 g of dried sample, spiked with 1 mg of ^{35}Cl-enriched

194   sodium chloride carrier (Source: Icon Isotopes, ^{35}Cl 99.635 atom %, ^{35}Cl/^{37}Cl = 273) to

195   measure native chloride by isotope dilution. A slurry of the sample and 120 g of deionized

196   water was slowly dissolved with 60 g of concentrated trace-metal grade nitric acid. Post-

197   dissolution, both liquid and undissolved solids were quantitatively transferred to a centrifuge

198   bottle where the solids were removed by centrifugation. The supernatant was decanted to

199   another centrifuge bottle and chloride was precipitated using one molar silver nitrate. After a

200   settling period, the bottle was centrifuged to isolate the silver chloride which was then

201   washed, dissolved with ammonium hydroxide, and treated with barium nitrate to remove

202   sulfate in preparation for further purification by chromatography. The solution was loaded

203   onto 5 ml of Bio-Rad AG 1-X8 strong anion-exchange resin and chloride was moved through

204   with 0.50 mmol, and then 0.150 mmol, nitric acid. After re-precipitation with silver nitrate

205   and a washing step the silver chloride was dried and packed into silver bromide-cored copper

206   holders. AMS measurements were performed at the Purdue Rare Isotope Measurement

207   Laboratory according to procedures in Muzikar et al. (2003); standards used for the

208   measurement are described in Sharma et al. (1990).

209

210   We applied a model developed by Schlagenhauf et al. (2010) for the interpretation of

211   earthquakes from cosmogenic ^{36}Cl concentrations to the Sparta fault scarp. This model

212   accounts for various parameters that control the ^{36}Cl concentration in a limestone normal

213   fault scarp, including geomagnetic field variations, host rock and hanging wall colluvium

214   chemical compositions and densities, scarp erosion rate, shielding of the scarp base by a

215   colluvial wedge, and the geometries of the fault scarp, the slope above the scarp, and the

216   hanging wall colluvial wedge. Their model uses three statistical parameters, the weighted root

217   mean square (RMSw), the reduced Chi-square (χ^2_{red}), and Akaike Information Criterion

218   (AIC) to assess the quality of fit between modelled and measured data to provide an objective

219   assessment of the number, and spatial and temporal spacing, of inferred earthquakes. For our

220   age calculations, we used the sea-level high-latitude (SLHL) ^{36}Cl production rate from

221   spallation in calcite of 59.4 atoms g^{-1} yr^{-1} and a temporally variable geomagnetic field to scale

222   the ^{36}Cl production rate from Lifton et al. (2005). A more recent ^{36}Cl production rate

223   calibration by Marrero et al. (2016) is not used here because it is scaled using Lifton et al.

224   (2014), which is not included in the model of Schlagenhauf et al. (2010). The Marrero et al.

225   (2016) production rate overlaps with the ^{36}Cl production rate from Lifton et al. (2005), within

226   uncertainty. We complemented the modelling of our new ^{36}Cl results with a re-modelling of

227   the Benedetti et al. (2002) data, using our own data for fault scarp and colluvium

228   composition. Our method of inferring earthquakes was based on fitting ^{36}Cl concentration

229   profiles derived from the Schlagenhauf et al. (2010) model to the actual ^{36}Cl concentration

230   profiles and inferring former soils surfaces from inflection points in the real ^{36}Cl

231   concentration profiles. This allows us to best constrain the paleoseismic history of the Sparta

232   fault over the late Holocene.

233

234   **3.2 Sparta fault scarp composition**

235   Fault scarp chemical composition and mineralogy were analyzed from the second sampling

236   profile, 50 m to the south of the first sampling profile, as follows. An initial elemental

237   analysis was done in the field on the Sparta fault scarp surface using an Olympus Innov-X

238   Delta (40 kV) handheld X-ray fluorescence (XRF) device. This instrument performs

239   elemental analyses with a circular sample spot of 8 mm diameter and can measure elements

240   heavier than Na. All elements lighter than Mg are reported as lighter elements (LE). Of the

241   elements that compose REY, it was only capable of measuring yttrium. Sampling was done at

242   an interval of 5 cm (or less) over a 7.7 m vertical profile, beginning ~90 cm below the

243   hanging wall soil surface. This profile corresponds with the location of the drill core and 2.0

244   m-long ^{36}Cl profiles but was measured before either drilling or slab sampling (Fig. 1c).

245

246   For more detailed analyses of elements, including REY, a total of 39 cores (22 mm and 35

247   mm diameters and to depths of ~4 cm) were collected every 20 cm from the fault scarp

248   vertical transect using a portable drill (Fig. 1d). The outermost 1 mm was removed from each

249   core prior to crushing to avoid contamination from the black surface coating. The next 15 mm

250   of each core were then rinsed with cold water, air dried, and crushed using a grinder with a

251   steel mortar to a grain size of <100 μm. This crushing technique might supply additional

252   REY to samples (Hickson and Juras, 1986) but if so, this likely occurs systematically across

253   samples and we are more interested in spatial trends, which we confirm independently using

254   the handheld XRF, than absolute abundances. The crushed samples were then analyzed for

255   major and trace elements using fusion inductively coupled plasma mass spectrometry (FUS-

256   ICP-MS) at Activation Laboratories (Ontario, Canada).

257

258   We complemented the FUS-ICP-MS analyses with spot elemental analysis of one rock core

259   from 1.1 m above the scarp base to make a high-resolution determination of any spatial

260   variations in the scarp composition. This was done with an energy-dispersive X-ray

261   spectroscope (EDS) attached to an environmental scanning electron microscope (ESEM). We

262   used a Quanta FEG 650 with Oxford-Inka EDS, and the analysis was made in a high-vacuum

263   environment at 20 kV. The technique is incapable of detecting REY because their

264   concentrations are too low. Photomicrographs and backscatter images of pore spaces were

265   also taken using the ESEM. These analyses were completed at the Department of Geological

266   Sciences, Stockholm University.

267

268   **3.3 Sparta fault scarp mineralogy**

269   A modal analysis of mineral fractions was completed on thin sections taken from the

270   remaining 38 core samples. This was done by counting 1000 points on each thin section

271   (Hutchison, 1974) using a Pelcon automatic point counter, attached to a Leica (DM LSP)

272   optical microscope. This point counter comprises a stepping frame attached to a control box

273   (power supply) and is also connected to a computer for statistical analyses using Pelcon

274   software version 2. The point counting and mineral identification was made using an

275   objective working distance of 1.52 mm. The line section pre-set step-length was 0.3 mm and

276   the line section distance was 1.5–2 mm. The point counting permitted a detailed quantitative

277   analysis of the mineralogy of the Sparta fault scarp surface. This detailed mineralogy was

278   then compared with the chemical composition data to determine whether phases other than

279   the host limestone are present.

280

281   **3.4 Hanging wall soil chemistry and pH**

282   Soil chemistry and pH were measured in samples taken at ~10 cm intervals to a depth of ~90

283   cm in the pit excavated at the base of the Sparta fault scarp (Fig. 1c). The elemental analysis

284   was again done with the handheld XRF device. Indicator strips were used to measure pH

285   from mixtures of 1:1 mass ratio of soil:distilled water, and soil:1 M KCl (Sikora and Moore,

286   2014). These analyses help determine the vertical distribution of REY in the soil (using

287   yttrium as a proxy) and indicate how they might correlate with pH and the vertical

288   distribution of REY in the fault scarp below the soil surface.

289

290   **4 Results**

291

292   **4.1 Sparta fault ^{36}Cl concentrations**

293   The cosmogenic nuclide ^{36}Cl concentrations from our three profiles (Table S1) and the

294   original Benedetti et al. (2002) ^{36}Cl concentrations are compared in Figure 2. The lowest ^{36}Cl

295   concentrations occur in our drill-core samples. Whereas age reversals are non-apparent in this

296   profile, comprised of widely dispersed sample points, there is a clear decrease in ^{36}Cl with

297   depth, including below the soil surface. Our 2.0 m- and 3.9 m-long profiles display

298   corresponding trends with increasing concentrations with increasing height on the fault scarp.

299   Only at 1.6 m do the trends strongly deviate from each other. The 2.0 m-long profile indicates

300   generally lower ^{36}Cl concentrations including six of 19 points that do not overlap within

301   uncertainty of data points at corresponding elevations on the 3.9 m-long profile. Four of those

302   points are located from 1.0 m to 1.3 m. In comparison with our 3.9 m-long profile, the

303   adjacent segment of the Benedetti et al. (2002) profile shows ^{36}Cl concentrations that are on

304   average 19% higher (0-4 m). Uncertainties (1σ) for data points comprising each profile are

305   almost identical, displaying a mean of 3.8% for the Benedetti et al. (2002) profile versus

306   3.9% for our 3.9 m-long and 2.0 m-long profiles. However, the Benedetti et al. (2002) profile

307   displays more variation between adjacent sample points than is evident in our profiles.

308   Whereas concentrations differ between the three longest profiles, they show a consistent

309   gradient up to ~4 m on the scarp face equivalent to an average uplift rate of 1.0–1.3 mm yr^{-1}.

310 Above 4 m on the scarp, both our drill-core profile and the Benedetti et al. (2002) profile

311 display matching lower gradients, which indicates a lower average uplift rate of 0.6–0.9 mm

312 yr^{-1}. If uplift rates are alternatively calculated as occurring prior to the subaerial exposure of

313 the lowermost samples by the most recent earthquake, cumulative uplift rates increase to 2.8

314 mm yr^{-1} and 1.8 mm yr^{-1} for the lower parts of the 3.9 m-long and Benedetti et al. (2002)

315 profiles, respectively. Both our 2.0 m-long and 3.9 m-long profiles indicate a local low in

316 ^{36}Cl concentration at ~0.5 m above the ground surface, which is opposite to the Benedetti et

317 al. (2002) profile, where concentrations reach a local high at ~0.5 m. Both of our profiles also

318 display an age reversal at 1.4–1.6 m, which is comparable to the age reversal at 1.2–1.5 m on

319 the Benedetti et al. (2002) profile. Our 3.9 m-long profile and the Benedetti et al. (2002)

320 profile each display additional age reversals at 2.6–2.7 m and 3.1–3.2 m on the scarp.

321 Another reversal is also apparent at 3.7–3.9 m in both profiles (including the drill-core

322 sample at 4 m). These reversals complement the gradients in being similarities shared by the

323 profiles that are key characteristics for a further analysis of its paleoseismicity using the

324 model of Schlagenhauf et al. (2010).

325

326 Using the Schlagenhauf et al. (2010) model, we analyze the number, ages, and magnitudes of

327 earthquakes inferred from a composite ^{36}Cl concentration profile; principally this record

328 contains the 3.9 m profile, but also includes the subsurface samples from our drill-core

329 profile, and the drill-core samples from 4.1 to 6.4 m (Fig. 3a). The total length of this record

330 then becomes 7.2 m. To match these two data sets, we increase the concentration of each drill

331 core sample by 5%. Integrating these two data sets is necessary to generating fits to the ^{36}Cl

332 data because subsurface data are required by the Schlagenhauf et al. (2010) model. The 5% is

333 chosen to match the ^{36}Cl concentrations in the four drill core samples between 0.8 m and 2.4

334 m with those in the corresponding segments of the 2.0 m and 3.9 m profiles, while

335   maintaining subsurface ^{36}Cl concentrations below those in the samples at 0.1 m on the 2.0 m

336   and 3.9 m profiles. Then, using the same parameters that generated the best model fit to the

337   3.9 m-long plus drill-core profile (Table 1), we apply the best model fit to our 2.0 m-long

338   profile (Fig. 3b) and the Benedetti et al. (2002) profile (Fig. 3c). In both cases, we use the

339   adjusted subsurface data from the drill-core profile. For our 2.0 m plus subsurface drill core

340   profile, we used the scarp mineralogy measured for each sample. For the 3.9 m-long plus drill

341   core profile and the Benedetti et al. (2002) plus subsurface drill core profile we used a mean

342   composition from our measured scarp mineralogy because we did not determine mineralogies

343   along these profiles. We further compare earthquakes modelled from age reversals in the ^{36}Cl

344   data with earthquakes modelled from potential soil profiles mirrored in scarp geochemistry

345   (REY, SiO$_2$ and Al$_2$O$_3$; Fig. 3d). We then use all data to infer the most likely earthquake

346   history for this segment of the Sparta fault.

347

348   From the combined 7.2 m-long profile, modelling indicates that five earthquakes at 1.4 m

349   (2.3 kyr B.P.), 2.6 m (2.8 kyr B.P.), 3.9 m (3.2 kyr B.P.), 5.1 m (3.8 kyr B.P.), and 6.5 m (5.9

350   kyr B.P.) provide the best statistical fit to our data (Fig. 3a; Table 1). Our best fit parameters,

351   taken either directly from field measurement or assumed (in the case of ε and pre-exposure),

352   are listed in Table 1. The two inferred earthquakes at 1.4 m (2.3 kyr B.P.) and 2.6 m (2.8 kyr

353   B.P.) also provide a good statistical fit to our 2.0 m-long profile (Fig. 3b). An inferred five

354   earthquakes on the Benedetti et al. (2002) profile (Fig. 3c) at the same elevations on the scarp

355   as our adjacent composite profile (Fig. 3a) display a statistically weaker fit than obtained for

356   our data (Table 1). Older ages and longer exposure prior to the oldest earthquake (pre-

357   exposure) are necessitated by the systematically higher ^{36}Cl concentrations. Earthquakes

358   inferred from the record of scarp geochemistry (Section 4.3) occur at 0.8 m (1.9 kyr B.P.), 2.6

359   m (2.8 kyr B.P.), 4.0 m (3.0 kyr B.P.), and at 6.4 m (5.9 kyr B.P.) on our 7.2 m-long profile

360   (Fig. 3d). Interestingly, this reconstruction has a statistically weaker fit than for earthquakes

361   inferred from reversals in ^{36}Cl concentrations (Fig. 3a; Table 1). We note that for the

362   applicable ^{36}Cl concentration profiles, model fits overestimate ^{36}Cl concentrations at 4 m on

363   the scarp surface (Figs. 3a, c, and d). In Figure 3a, c, and d, an (artificial) earthquake is added

364   to the top of the ^{36}Cl concentration profile to fit all data (Earthquake 1, shown in grey).

365   Because this oldest earthquake is tied to the highest sample on the scarp, without an

366   associated age reversal, and because ^{36}Cl measurements are sparely spaced above 4 m, the

367   inferred locations on the fault scarp and timing of this earthquake are approximate. We

368   therefore focus our interpretations on the inferred earthquakes lower down on the fault scarp.

369

370   The model fit to our data is sensitive to input parameters, at least two of which are difficult to

371   accurately measure (Fig. 4). It is most sensitive to the scarp dip angle (e.g., a 5° decrease

372   causes the AICc to increase by 12%), followed by the density of colluvium mantling the

373   hanging wall and the rate of scarp surface erosion. It is least sensitive to variations in rock

374   density and hillslope gradient. The colluvium density depends on relative abundances of

375   limestone clasts, mineral soil, organic matter, and water, which vary spatially. Due to, for

376   example, wetting and drying, colluvium density is expected to also vary temporally. Scarp

377   erosion rates remain undetermined. The adopted values for colluvium density and scarp

378   erosion rate are, therefore, those which provide the best model fits to the data. In both cases,

379   those values are also realistic (Table 1). Rock density is prescribed from the literature and

380   colluvium dip, scarp dip, and hillslope gradient are based on measurements. Optimal

381   colluvium and scarp dips are adjusted slightly relative to measured values (i.e., 1–2°, which is

382   within measurement uncertainty).

383

384   **4.2 Granulometry of the Sparta fault scarp surface**

385   A first look at the Sparta fault scarp surface yields a misleading impression of homogeneous

386   limestone (Figs. 1, 5a), whereas close inspection of the core samples instead reveals a typical

387   fault breccia (Figs. 5b-d). This breccia consists of angular-to-rounded limestone clasts with

388   axes of 1–7 mm (in the two-dimensional view provided by thin sections) surrounded by

389   matrix/cement in which clasts are <0.1 mm in length. The fault breccia is defined as a

390   protocataclasite, according to the classification of Woodcock and Mort (2008). The

391   composition of the protocataclasite displays large spatial variations, with some portions

392   containing abundant clasts (Fig. 5c), whereas others are dominated by fine matrix (Fig. 5d).

393   The proportion of clasts >2 mm ranges from 5% to 20% vertically along the fault scarp and

394   the proportion of matrix ranges from 5% to 60%. We did not measure the thickness of the

395   protocataclasite but it everywhere exceeds the 4 cm depth of our drill cores.

396

4.3 Sparta fault scarp composition and mineralogy

398   In addition to a spatially variable granulometry, the fault scarp shows a spatially variable

399   distribution of major and trace elements. The major component is, as expected for limestone,

400   CaO (mean 52.22%) but its concentration varies between 43.83% and 56.64% (Table S2),

401   which exceeds spatial variations in CaO seen elsewhere in limestone normal fault scarps

402   (Carcaillet et al., 2008; Tesson et al., 2016). Quartz (SiO_2) also occurs, and it too displays

403   spatial variations (0.10%–20.82%), with broad peaks occurring at -0.5– -0.4 m, 0.9–1.2 m,

404   4.6–4.8 m, and 6.0–6.2 m along the vertical fault scarp profile (Fig. 6; Table S2). An

405   additional peak in SiO_2, but which is not seen in point counting of quartz, occurs at 6.2 m

406   (Fig. 6; Tables S2 and S3). Mean concentrations of other major elements are low in bulk

407   samples, including Al_2O_3 (0.21%), MgO (0.16%), Fe_2O_3 (0.09%), P_2O_5 (0.07%), and K_2O

408   (0.05%; Table S2). However, EDS measurements, such as shown in Figure 7a, reveal that the

409   concentrations of some elements are frequently much higher in intergranular pores (Fig. 7c)

410   than elsewhere in the fault scarp, including Si ≤ 38.3%, Al ≤ 11.7%, Fe ≤ 48.4%, and K ≤

411   7.1% (Table S4). Furthermore, intergranular pores and quartz frequently occur together (Fig.

412   7b) and the concentration of Al_2O_3 covaries with the much more abundant quartz (SiO_2) (Fig.

413   6).

414

415   Quartz is revealed by microscopy to be present as randomly oriented rounded-to-angular

416   grains that are <50 μm in diameter (Figs. 5d, 7b). Quartz is a constituent of the

417   protocataclasite fine matrix that is mostly comprised of microcrystalline calcite precipitates

418   and which cements larger host rock-derived $CaCO_3$ clasts (Figs. 5b-d, 7b, 8a). Point counting

419   further reveals quartz modes ranging from 0.1% to 15.4% of thin section area (Table S3),

420   with higher abundances correlating to higher abundances of fine matrix. The spatial

421   correlations between SiO_2, quartz abundances on point counting, and fine matrix are further

422   indicated by the EDS spot elemental analysis (Fig. 8). Here, the two selected spots in the fine

423   matrix display Si abundances of 29.7% and 28.9%, which contrasts with 1.7% and 0.9% for

424   the two spots located on clasts. CaO abundances display an inverse relationship with SiO_2

425   (33.7% and 31.2% for the clasts versus 4.8% and 5.1% for the fine matrix). SiO_2 is present

426   largely as quartz, as evidenced by the strong spatial correlation between quartz and SiO_2

427   along the vertical profile (Fig. 6). Quartz can therefore be used as a proxy for fine matrix

428   abundances in the Sparta fault scarp.

429

430   In addition to the spatial relationship between quartz and fine matrix, we observed in

431   backscatter SEM images that pore spaces, which frequently harbor higher concentrations of

432   Si, Al, K and/or Fe than host rock-derived clasts, are also more abundant in the fine matrix

433   (Fig. 7c). These observations provide evidence that clay particles (< μm-scale) frequently

434   coat pore spaces. The abundance of quartz therefore also provides a proxy for the abundance

435   of clay-coated pore spaces.

436

437   Concentrations of yttrium are generally low (1.2–11.1 ppm; Table S5) but vary in a wave-like

438   pattern along the vertical profile, with maxima occurring at -0.4 m, 0.8 m, 2.6 m, 4.0 m, and

439   6.4 m (Fig. 9). These maxima do not systematically decrease with vertical distance above the

440   hanging wall and are not highest in the soil-mantled portion of the scarp. Yttrium (mean 6.3

441   ppm), La (mean 5.04 ppm), Nd (mean 3.54 ppm), and Ce (mean 2.31 ppm) have the highest

442   concentrations, whereas all other REY are <1 ppm (Table S5). The concentrations of REY

443   elements co-vary vertically along the scarp surface ($R^2 = 0.95$; Fig. 9), the proportion of

444   light-REY (LREY) to heavy-REY (HREY) remains constant (ratio ~7:1; Fig. 10; Table S5),

445   and concentration maxima occur at locations that correspond closely with the Al_2O_3 maxima

446   (Fig. 9; Table S5). Accordingly, there is a strong correlation between REY and Al_2O_3 ($R^2 =$

447   0.92; Fig. S2a). Spatial correlations between REY and SiO_2 and K_2O are also observed ($R^2 =$

448   0.56 and 0.87, respectively; Fig. S2c, e). In contrast, the locations of REY maxima correlate

449   neither with the location of the present ground surface (-0.4 m) nor former ground surfaces at

450   1.4 m and 5.1 m inferred from [36]Cl data. There are, however, correlations between REY

451   maxima and former ground surfaces at 2.6 m, 3.9–4.0 m, and at 6.4–6.5 m modelled from the

452   [36]Cl data. No systematic relationship is therefore apparent between REY maxima and either

453   the present soil surface or former soil surfaces inferred from inflection points in [36]Cl

454   concentrations.

455

456   **4.4 Hanging wall soil chemistry and pH**

457   The terra rosa soil mantling the hanging wall primarily comprises aeolian dust (Muhs et al.,

458   2010) and carbonate clasts. At our sample site, the soil thickness at the base of the Sparta

459   fault scarp is 0.8 m and this appears to be stable, at least over the timescale of scarp surface

460   dissolution, as evidenced by a much smoother scarp surface texture below the soil surface

461   compared with the subaerially exposed scarp. Below the organic horizon (~0.1 m thick) the

462   soil is welded, probably by calcite precipitates, and horizons are absent. Soil pH is, in

463   general, slightly acidic along the excavated vertical profile, remaining within a 6.2 to 7.0

464   range (Fig. 11a; Table S6). An outlier occurs at -0.30 m, where the pH is 5.6 ± 0.2. Soil

465   composition varies with depth (Fig. 11b; Table S7). Concentrations of Si, Al, and K are lower

466   in the organic horizon (11%, 0–5%, and 0.4%, respectively) compared with the remainder of

467   the profile (18%–30%, 5–10%, and 0.5–0.9%, respectively), whereas the concentrations of

468   LE, which includes C, are, as expected, higher in the organic horizon (75%–80%) than in the

469   lower profile segment (51%–64%). The concentration of yttrium ranges from a maximum of

470   36–39 ppm at -0.5– -0.6 m depth to a minimum of 11 ppm at -0.1 m depth and its vertical

471   distribution correlates positively with Si ($R^2 = 0.71$), Al ($R^2 = 0.45$), and K ($R^2 = 0.54$), but

472   negatively with pH ($R^2 = -0.52$; Figs. 11c, S1b,d,f; Table S7).

473

474   **5 Discussion**

475

476   **5.1. Modelling of earthquakes from ^{36}Cl concentration profiles**

477   Our modelling using Schlagenhauf et al. (2010) indicates that five earthquakes provide a best

478   fit to the Sparta fault ^{36}Cl data. The youngest inferred earthquake (2.3 kyr B.P.) corresponds

479   both with the historical 464 B.C.E. event and inflections in the ^{36}Cl data of the 2.0 m-long

480   and 3.9 m-long profiles. The penultimate inferred earthquake at 2.8 kyr B.P. correlates to an

481   inflection in ^{36}Cl concentration at 2.6 m in our 3.9 m-long profile. Because data density

482   decreases above 4.0 m, there are no clear inflections in ^{36}Cl concentrations to base the

483   occurrence of earthquakes on for this segment of the scarp. However, fitting the

484   Schlagenhauf et al. (2010) model to the measured gradient in ^{36}Cl concentrations yields an

485   additional record of three older earthquakes at 3.2 kyr B.P., 3.8 kyr B.P., and 5.9 kyr B.P. to

486   explain the exhumation of the exposed scarp surface. The four most recent earthquakes are

487   clustered within a 1.5 kyr period, whereas nearly 2.5 kyr have elapsed since the last

488   earthquake on the Sparta fault. A lower gradient in ^{36}Cl concentration on the fault scarp

489   above the location of the inferred 3.2 kyr B.P earthquake also indicates a lower rate of scarp

490   exhumation prior to the 1.5 kyr period of apparently higher earthquake activity. The long

491   recent quiescent interval therefore does not necessarily provide evidence that another (large

492   magnitude) earthquake may be imminent. As a comparison, extensional faults in the central

493   Italian Apennines accumulate meters of displacement over several thousands of years, but

494   also display similar length periods where cumulative slip magnitudes are much lower,

495   because earthquake activity shifts between faults across-strike (Cowie et al., 2017). The same

496   may also apply to the Sparta fault and related extensional faults in the region.

497

498   The precision at which we can interpret paleoseismicity is constrained by three factors. These

499   include (i) sparse ^{36}Cl data above 4.0 m on the Sparta fault scarp, (ii) uncertainties in scarp

500   erosion rate, pre-exposure length, and hanging wall surface dip angle and colluvium density

501   (Fig. 4), and (iii) fault scarp impurities that produce noise in the ^{36}Cl data and distortion of

502   potential REY indicators of former soil surfaces. Below, we will explore methodological and

503   geological sources of uncertainty in the ^{36}Cl data, reasons for mineralogical impurities in the

504   Sparta fault scarp, and how the observed REY distribution can be interpreted. This will be

505   achieved by comparing the 2.0 m-long profile with the equivalent segment of the 3.9 m-long

506   profile because both profiles have been sampled, processed, and analyzed in the same manner

507   and at the same time, and therefore provide a measure of repeatability.

508

5.2 Methodological and geological sources of uncertainty in the ^{36}Cl data

A peculiar feature of the ^{36}Cl data is that the profile comprised of small drill-core samples

generally yields younger exposure ages for the Sparta fault scarp than the 2.0 m- and 3.9 m-

long profiles, which, in turn, are systematically younger than the Benedetti et al. (2002)

profile (Fig. 2). The Benedetti et al. (2002) profile displays variations between adjacent

sample points that exceed those observed in our profiles and rival variations in ^{36}Cl

concentrations that may be attributable to earthquakes. We interpret the systematic

differences in ^{36}Cl concentration between the drill-core profile, the 2.0 m and 3.9 m profiles,

and the Benedetti et al. (2002) profile as reflecting methodological differences related to

advances in sample preparation chemistry at PRIME-Lab, Purdue University. Similarly, the

reason why we can directly infer the 464 B.C.E earthquake at Anogia, in contrast to Benedetti

et al. (2002), is attributable to advances in age calculations from ^{36}Cl concentrations.

Whereas our 2.0 m- and 3.9 m-long profiles display corresponding trends with increasing

elevation on the fault scarp, the 2.0 m profile has generally lower ^{36}Cl concentrations (Fig. 2).

Indeed, six of its 19 ^{36}Cl concentrations do not overlap within uncertainty with concentrations

of corresponding samples on the 3.9 m profile, including four points located between 1.0 m

and 1.3 m. We interpret these differences as indicating that the fault scarp of the 2.0 m profile

has been either partly shielded from cosmogenic radiation, has eroded more than the surface

of the 3.9 m profile, or contains a higher concentration of impurities. Of potential additional

relevance is that the texture of the scarp surface at the location of the 2.0 m profile is

smoother than at the location of the 3.9 m profile. Because a similarly smooth texture also

characterizes the scarp surface presently buried by colluvium mantling the hanging wall, the

smooth texture at the location of the 2.0 m profile may indicate either recent burial of the

scarp surface by colluvium and/or $CaCO_3$ dissolution occurring at a higher rate than at

534   locations where the exposed scarp surface texture is rougher. If a smooth texture reflects

535   erosion through $CaCO_3$ dissolution, there might be preferential flow, or seepage, of water

536   from the hillslope above the scarp at the location of the 2.0 m profile. Observed lumps of

537   colluvium cemented to the Sparta fault scarp, at locations perched above the present hanging

538   wall surface (Fig. S1) partially shield the underlying scarp surface. However, had this

539   previously occurred at the location of our 2.0 m profile, an eroded colluvial lump would be

540   evidenced in the hanging wall sediments. On the contrary, there is no colluvial lump, but

541   rather a sub-horizontal surface is present with an expression that differs little from the surface

542   below the 3.9 m profile. The inter-profile differences in ^{36}Cl concentrations illustrate the

543   value in taking samples for ^{36}Cl measurements from more than one vertical profile, because

544   evidence of past shielding by sediments or bedrock can otherwise be difficult, at best, to

545   detect. Partial shielding may impact the interpretation of the number of paleoearthquakes and

546   result in lower age estimates of earthquakes, with a corresponding decrease in recurrence

547   intervals.

548

549   **5.3. The effects of mineralogical impurities on ^{36}Cl concentration profiles**

550   Mineralogical impurities embedded in the fault breccia that comprises the scarp surface

551   appear to be a key geological reason for spatial variations in the concentration of ^{36}Cl. This

552   effect is best evidenced when comparing modelled ^{36}Cl concentrations for the 2.0 m-long

553   profile (Fig. 3b), including measured mineralogy for each sample location, with modelled

554   ^{36}Cl concentrations for the 3.9 m-long and Benedetti et al. (2002) profiles, including mean

555   values of the scarp composition derived from our measured data (Fig. 3a, c, d). Whereas the

556   latter modelled profiles appear smooth, the modelled 2.0 m profile contains inter-sample

557   noise, which reflects variations in calcite abundance, attributable to the additional, and

558   variable, presence of quartz and other minerals, including trace amounts of clay lining pores

559   (Figs. 5–9). Because ^{36}Cl is also produced by spallation on K (162 ± 24 atoms g^{-1} yr^{-1} at

560   SLHL; Evans et al., 1997), Fe (1.9 ± 0.2 atoms g^{-1} yr^{-1} at SLHL; Stone, 2005), and Ti (13 ± 3

561   atoms g^{-1} yr^{-1} at SLHL; Fink et al., 2000), noise in the ^{36}Cl data might also partly reflect the

562   relative abundances of these elements. However, for the case of the Sparta fault, this appears

563   to be insignificant given that measured concentrations of these elements are extremely low

564   (concentrations of K$_2$O, Fe$_2$O$_3$, and TiO$_2$ are 0–0.12%, 0.03–0.24%, and 0–0.02%,

565   respectively; Fig. S3, Table S2).

566

567   Mineralogical impurities may also explain two other enigmatic features in the ^{36}Cl data.

568   Firstly, an apparent age reversal occurs at 3.1 m in the 3.9 m-long profile (Fig. 3a). Although

569   this could indicate the location of a former soil horizon and thus inferred displacement by an

570   earthquake, a better model fit is gained by locating an earthquake higher up the scarp at 3.9

571   m. Secondly, ^{36}Cl concentrations at ~4 m in the 3.9 m profile and the Benedetti et al. (2002)

572   data (3.8-4.1 m, Fig. 3a; 3.7-4.3 m, Fig. 3c) are too low to overlap within uncertainty with

573   concentrations modeled using Schlagenhauf et al. (2010). A possible explanation for both

574   enigmatic features is an inability to fully capture the effects of mineralogical impurities on

575   ^{36}Cl production rates. This is largely because, in the absence of mineralogical data for these

576   profiles, we have calculated a mean composition based on the mineralogical data for the 2.0

577   m profile to model ^{36}Cl concentrations. However, even with the mineralogical data, current

578   laboratory techniques for preparing samples for ^{36}Cl measurement may not record

579   mineralogical variations at sufficient precision. In addition to highlighting the importance of

580   mineralogical analyses, we also highlight the value of using a model to identify the likely

581   displacements by paleoearthquakes through fitting model ^{36}Cl concentration profiles to real

582   ones, rather than overtly relying on apparent age reversals. It remains possible that two

583   earthquakes occurred in close succession, but with this data and methodology, we cannot

584   confidently infer both of those.

585

5.4. Estimated magnitude of the 464 B.C.E. earthquake

587   The 464 B.C.E. earthquake that destroyed Sparta had an estimated moment (M_o) of $1 - 4$ (x

588   10^{19}) N m. This is derived from multiplying the vertical displacement of 1.4 m (Fig. 3a-c)

589   with fault dimensions of 20 x 14 km – 64 x 14 km, and with a shear modulus of 3.23×10^{10} N

590   m^{-2} (Armijo et al., 1991). The values of 20 km, 14 km, and the shear modulus are from

591   Armijo et al. (1991) and 64 km is the mapped length of the Sparta fault in Figure 1. This

592   estimated range of M_o values straddles a previous "most probable" estimate of moment by

593   Armijo et al. (1991) of 3×10^{19} N m even though they lacked field constraints on fault slip

594   distance during the Sparta Earthquake. Hence, we conclude from this congruence of the

595   probable value with values based on the vertical displacement modelled from the ^{36}Cl data

596   (Fig. 3), that they are reliable. From the empirically derived equations of Pavlides and Caputo

597   (2004) and a vertical displacement of 1.4 m of the Sparta fault, we calculate a magnitude (M_s)

598   of 6.8-7.2 for the 464 B.C.E. earthquake. Given the severe destruction inflicted upon the

599   Spartan society (REF?), we consider that the upper estimate is most likely. A magnitude 7.2

600   earthquake is also in agreement with the estimate by Armijo et al. (1991), although they

601   based this on ~10 m of vertical displacement. We are less certain of the magnitudes and

602   timing of older earthquakes. However, it appears that the Sparta fault was exhumed by a

603   series of similarly large earthquakes over a period of about 3.5 kyr.

604

5.4. Interpretation of REY distributions

606   REY cannot be used to infer imprints of former soil profiles on the Sparta fault at Anogia.

607   Petrographic analyses indicate that the Sparta fault scarp is composed of a protocataclasite

608   consisting of calcite clasts derived from the host limestone, microcrystalline calcite cement,

609   and quartz (Figs. 5, 6). Furthermore, EDS analysis indicates that trace amounts of clay, such

610   as illite, are lining pores where microcrystalline calcite cement and quartz are located (Fig. 7;

611   Carcaillet et al., 2008). Given the correlations between REY and each of Al, K, and Si (R^2 =

612   0.92, 0.87, and 0.56, respectively; Fig. S2a-c), we infer that the clays embedded in the fault

613   scarp are hosting REY. This is a likely explanation for why REY peaks 0.4 m below the

614   current soil surface (Fig. 9), rather than at the soil surface as has been observed on the

615   Magnola fault in Italy (Manighetti et al., 2010).

616

617   The formation of protocataclasite occurs beneath the Earth's surface at depths that may range

618   from meters to up to thousands of meters. A model for this involves fluids moving along the

619   Sparta fault, primarily associated with seismic events. These fluids dissolve $CaCO_3$ from the

620   host-limestones and potentially also silicate minerals from psammitic and pelitic

621   (meta)sediments, where they are dissected by the fault. In association with variations in

622   temperature and pressure along the fault, chemical saturation of these fluids results in

623   precipitation of clay, quartz, and microcrystalline calcite, which cements clasts of host-rock

624   derived limestone into the fault breccia. Subsequent faulting re-fractures the breccia and

625   particle comminution over time produces quartz grains that are rounded-to-angular in shape,

626   randomly oriented, and <50 μm (Figs. 5, 7). The fault breccia may also have undergone

627   multiple generations of microcrystalline calcite re-cementing from re-circulating fluids. As an

628   alternative to a dissolution-precipitation model, clay and quartz emplacement may involve

629   fluid entrainment of particles and grains from clay- and quartz-bearing sedimentary units

630   during faulting, as has been observed elsewhere (e.g., Darwin, 1840; Roy, 1946; Brandon,

631   1972; Röshoff and Cosgrove, 2002). This process may also be accompanied by comminution

632   of fault-zone quartz grains derived from psammitic rocks. We tentatively exclude a

633   contemporary aeolian source for the clay and quartz because there is no documented

634   mechanism to transport clay particles and quartz grains from the soil to centimeters into a

635   fault scarp. We cannot distinguish soil to scarp clay and quartz migrations on the Sparta fault

636   which has been observed, for example, at the micrometer scale in surface coatings on the

637   Magnola fault, because that scarp is comprised of pure carbonate (Carcaillet et al., 2008). It is

638   likely that limestone fault scarps are generally composed of fault breccias (Agosta and Aydin,

639   2006; Carcaillet et al., 2008; Nuriel et al., 2012) and that where a fault intersects varying

640   lithologies, chemical and mineralogical heterogeneities may occur in the fault breccia, as

641   observed on the Sparta fault. Where they occur, these heterogeneities may control the spatial

642   distribution of REY, independent of any spatial reorganization of REY attributable to

643   subaerial weathering.

644

645   REY correlates with inferred clay abundances on the Sparta fault scarp (Fig. 9), rather than

646   systematically with former soil profiles inferred from [36]Cl concentrations. A correlation of

647   REY with Si and Al is indeed observed in the soils mantling the Sparta (R^2 = 0.71 and 0.45,

648   respectively; Figs. 11c and S2b,c), Kaparelli (R^2 = 0.95 for Si; Figs. 1a and S4a), and

649   Magnola fault hanging walls (R^2 = 0.98 for both Si and Al; Fig. S4b,c and electronic

650   appendix to Manighetti et al., 2010). These correlations generally contrast with a weaker

651   negative correlation between Y and pH (R^2 = 0.52) for the hanging wall soil on the Sparta

652   Fault (Fig. 11c). We propose a causative relationship between the vertical distributions of

653   REY and clay on the Sparta fault scarp. The presence of clay likely relates to fault breccia

654   formation at considerable depths beneath the Earth's surface, rather than subaerial weathering

655   processes. This reasoning is supported by the following observations:

656   *(i)*   The Sparta fault scarp REY concentrations are equivalent to (Nuriel et al., 2012;

657   Goodfellow et al., 2017) or higher than those measured elsewhere in platformal

658   limestone (Carcaillet et al., 2008; Mouslopoulou et al., 2011), but yttrium

659   concentrations are lower than in the adjacent hanging wall soil (rare-earth elements

660   were not measured; Tables S5, S7).

661  *(ii)* If REY exchange between the soil and fault scarp occurs according to the Carcaillet

662   et al. (2008) model, fractionation of LREY and HREY elements is expected. For

663   example, LREY might be preferentially mobilized (Takahashi et al., 2005;

664   Carcaillet et al., 2008), leading to an enrichment of LREY relative to HREY in the

665   fault scarp, where there are peaks in total REY. Conversely, LREY may be depleted

666   relative to HREY where there are troughs in total REY. However, the proportion of

667   LREY to HREY remains constant vertically along the Sparta fault scarp (Fig. 10).

668  *(iii)* There is no systematic decrease in total REY along the vertical scarp profile (Fig.

669   9), in contrast to declining concentrations with distance above the hanging wall on

670   the Magnola fault (Carcaillet et al., 2008).

671 Whereas these observations discount subaerial weathering as the dominant mechanism for

672 REY enrichment and depletion on the Sparta fault, there may be some weathering-induced

673 exchange. This is evidenced by the peak in REY on the buried Sparta fault scarp correlating

674 with the peak in soil acidity (Figs. 9, 11a, b), but which notably occurs in the subsurface,

675 rather than at the soil surface. If, as we infer, the spatial patterning of REY, quartz, and clay

676 (as indicated by Al) is inherited from depth, the observed wave-like signal (Figs. 6, 9) may

677 reflect sorting and cementing of breccia around surface asperities on the fault plane. The

678 resulting infilling of depressions with fault gauge may create a successively more polished

679 and localized fault plane along which friction is lowered, thereby permitting larger slip (i.e.,

680 larger earthquakes) along the fault (Sagy and Brodsky, 2009). Whereas REY concentrations

681 do not appear to be a reliable indicator of Holocene paleoseismicity along the Sparta fault,

682 they may instead reveal processes that localize slip to a discrete fault plane.

683

6 Conclusion

685

686 In applying cosmogenic ^{36}Cl exposure-age dating and rare-earth elements and yttrium (REY)

687 measurements to unravelling the paleoseismic history of the Sparta fault, Greece, we

688 conclude the following: Modeling of ^{36}Cl concentrations along two vertical profiles on the

689 Sparta Fault, closely adjacent to a ^{36}Cl concentration profile previously measured and

690 interpreted by Benedetti et al. (2002), indicates that the scarp was likely exhumed over 5

691 earthquakes, including one at ~2.3 ± 0.2 kyr B.P., which correlates with the 464 B.C.E. event.

692 Four earthquakes were clustered within a 1.5 kyr period that culminated with the 464 B.C.E.

693 event. Cumulative uplift was as high as 2.8 mm yr^{-1} during that period, compared with ~0.6–

694 0.9 mm a^{-1} over the preceding 2.7–4.4 kyr. Because earthquake activity may shift between

695 faults in extensional settings, a large magnitude earthquake is not necessarily indicated as

696 being overdue by the ~2.5 kyr that have elapsed since the 464 B.C.E. event. More generally,

697 accurate identification of individual earthquakes is presently constrained by spatial variations

698 in ^{36}Cl concentration profiles that reflect neither exposure duration nor imprints of former soil

699 profiles. In cases where this is attributable to mineralogical variations, such as in the Sparta

700 fault scarp, present chemical preparation techniques for AMS measurement of ^{36}Cl may

701 insufficiently account for those variations.

702

703 The Sparta fault scarp is impure; it is composed of fault breccia, which contains quartz and

704 clay-lined pores in addition to calcite. The vertical distribution of REY is highly correlated

705 with the pore-clay and may indicate processes of fault evolution deep below the ground

706 surface. The potential exchange of REY between the hanging wall colluvium and the adjacent

707 footwall scarp is overwhelmed at this site by REY attached to the pore clays inherited from

708   depth. Because of this, Holocene earthquakes and their slip distances and magnitudes cannot

709   be inferred for the Sparta fault from REY concentrations. This is probably true also for

710   similar impure limestone fault scarps elsewhere.

Author contribution

711

712   AS conceived the study and AS, APS, MWC, RF, and BWG participated in fieldwork. RF

713   conducted the analysis of scarp composition, made initial interpretations, and compiled an

714   initial manuscript as a part of research studies at Stockholm University. BWG made

715   additional analyses, including earthquake modelling, and led writing of this manuscript. GC

716   led the laboratory preparation of samples for ^{36}Cl measurement, in which BWG also

717   participated. GC calculated ^{36}Cl concentrations from the AMS data. All authors contributed

718   to data interpretation and manuscript editing.

719

Competing interests

720

721   Arjen P. Stroeven is a member of the editorial board for Solid Earth.

722

Acknowledgements

723

724   We thank Mikael Amlert for his assistance with field safety and sampling, Giorgos Maneas,

725   station manager of the Navarino Environmental Observatory (NEO), for his extensive

726   assistance with field logistics, and our deceased friend, Dan Zetterberg, Department of

727   Geological Sciences, Stockholm University, for his assistance with thin section preparations.

728   This project was funded by the Stockholm University Research School for teachers focusing

729   on Natural Hazards financed by the Swedish Research Council and by a grant from NEO. We

730   gratefully acknowledge funding for fieldwork from the Swedish Society for Anthropology

731   and Geography Andreé Fund to Fritzon.

732

References

733

734   Agosta, F. and Aydin, A.: Architecture and deformation mechanism of a basin bounding

735   normal fault in Mesozoic platform carbonates, central Italy. Journal of Structural

736   Geology, 28, 1445–1467, 2006.

737   Armijo, R., Lyon-Caen, H., and Papanastassiou, D.: A possible normal-fault rupture for the

738   464 BC Sparta earthquake. Nature, 351, 137–139, doi: 10.1038/351137a0, 1991.

739   Benedetti, L., Finkel, R., Papanastassiou, D., King, G., Armijo, R., Ryerson, F., Farber, D.,

740   and Flerit, F.: Post-glacial slip history of the Sparta fault (Greece) determined by ^{36}Cl

741   cosmogenic dating: Evidence for non-periodic earthquakes. Geophysical Research

742   Letters, 29, 1246, doi: 10.1029/2001GL014510, 2002.

743   Brandon, A: Clastic dykes in the Namurian shales of County Leitrim, Republic of Ireland.

744   Geological Magazine, 109, 361–67, 1972.

745   Carcaillet, J., Manighetti, I., Chauvel, C., Schlagenhauf, A., and Nicole, J.-M.: Identifying

746   past earthquakes on an active normal fault (Magnola, Italy) from the chemical analysis of

747   its exhumed carbonate fault plane. Earth and Planetary Science Letters, 271, 145–158,

748   doi: 10.1016/j.epsl.2008.03.059, 2008.

749   Cowie, P.A., Phillips, R.J., Roberts, G.P., McCaffrey, K., Zijerveld, L.J.J., Gregory, L.C.,

750   Faure Walker, J., Wedmore, L.N.J., Dunai, T.J., Binnie, S.A., Freeman, S.P.T.H.,

751   Wilcken, K., Shanks, R.P., Huismans, R.S., Papanikolaou, I., Michetti, A.M., and

752   Wilkinson, M.: Orogen-scale uplift in the central Italian Apennines drives episodic

753   behaviour of earthquake faults. Scientific Reports 7, 44858, 2017.

754 Darwin, C: Geological observations in the volcanic islands and parts of South America
755   visited during the voyage of H.M.S. Beagle. London, 1840.
756 Dramis, F, and Blumetti, A.M.: Some considerations concerning seismic geomorphology and
757   paleoseismology. Tectonophysics, 408, 177–191, 2005.
758 Evans, J.M, Stone, J.O.H., Fifield, L.K., and Cresswell, R.G.: Cosmogenic chlorine-36
759   production in K-feldspar. Nuclear Instruments and Methods in Physics Research B, 123,
760   334–340, 1997.
761 Fink, D., Vogt, S., and Hotchkis, M.: Cross-sections for ^{36}Cl from Ti at $E_p = 35$–150 MeV:
762   Applications to in-situ exposure dating. Nuclear Instruments and Methods in Physics
763   Research B, 172, 861–866, 2000.
764 Godey, S., Bossu, R., and Guilbert, J.: Improving the Mediterranean seismicity picture thanks
765   to international collaborations. Physics and Chemistry of the Earth, Parts A/B/C 63, 3–11,
766   doi:10.1016/j.pce.2013.04.012, 2013.
767 Goodfellow, B.W., Viola, G., Bingen, B., Nuriel, P., and Kylander-Clark, A.: Paleocene
768   faulting in SE Sweden from U-Pb dating of slickenfiber calcite. Terra Nova 29, 321–328.
769   https://doi.org/10.1111/ter.12280, 2017.
770 Gürpinar, A.: The importance of paleoseismology in seismic hazard studies for critical
771   facilities. Tectonophysics, 408, 23–28, doi: 10.1016/j.tecto.2005.05.042, 2005.
772 Hickson, C.J. and Juras, S.J.: Sample contamination by grinding. Canadian Mineralogist 24,
773   585-589, 1986.
774 Hutchison, C.S.: Laboratory Handbook of Petrographic Techniques. Wiley-Interscience, New
775   York, 527 pp, 1974.
776 Institute for Geology and Subsurface Research: Sparti Sheet, photogeological map of Greece,
777   1969.
778 Jolivet, L., Faccenna, C., Huet, B., Labrousse, L., Le Pourhiet, L., Lacombe, O., Lecomte, E.,
779   Burov, E., Denèle, Y., Brun, J.-P., Philippon, M., Paul, A., Salaün, G., Karabulut, H.,
780   Piromallo, C., Monié, P., Gueydan, F., Okay, A.I., Oberhänsli, R., Pourteau, A., Augier,
781   R., Gadenne, L., and Driussi, O.: Aegean tectonics: Strain localisation, slab tearing and
782   trench retreat. Tectonophysics, 597–598, 1–33, 2013.
783 Lifton, N.A., Bieber, J.W., Clem, J.M., Duldig, M.L., Evenson, P., Humble, J.E., and Pyle,
784   R.: Addressing solar modulation and long-term uncertainties in scaling secondary cosmic
785   rays for in situ cosmogenic nuclide applications. Earth and Planetary Science Letters,
786   239, 140–161, 2005.
787 Lifton, N.A., Sato, T., Dunai, T.J.: Scaling in situ cosmogenic nuclide production rates using
788   analytical approximations to atmospheric cosmic-ray fluxes. Earth and Planetary Science
789   Letters, 386, 149–160, 2014.
790 Lifton, N.A., Smart, D.F., Shea, M.A.: Scaling time-integrated in situ cosmogenic nuclide
791   production rates using a continuous geomagnetic model. Earth and Planetary Science
792   Letters, 268, 190–201, 2008.
793 Manighetti, I., Boucher, E., Chauvel, C., Schlagenhauf, A., Benedetti, L.: Rare earth elements
794   record past earthquakes on exhumed limestone fault planes. Terra Nova, 22, 477–482,
795   doi: 10.1111/j.1365-3121.2010.00969.x, 2010.
796 Marrero, S.M., Phillips, F.M., Caffee, M.W., Gosse, J.C.: CRONUS-Earth cosmogenic ^{36}Cl
797   calibration. Quaternary Geochronology, 31, 199–219, 2016.
798 McCalpin, J.P.: Paleoseismology, Academic press, 613 pp., 2009.
799 McDonough, W.F., and Sun, S.-s.: The composition of the Earth. Chemical Geology, 120,
800   223–253, 1995.
801 Michetti, A.M., Audemard M., F.A. and Marco, S.: Future trends in paleoseismology:
802   Integrated study of the seismic landscape as a vital tool in seismic hazard analyses
803   Tectonophysics, 408, 3–21, 2005.

804 Mitchell, S.G., Matmon, A., Bierman, P.R., Enzel, Y., Caffee, M., and Rizzo, D.:
805   Displacement history of a limestone normal fault scarp, northern Israel, from cosmogenic
806   Cl-36. Journal of Geophysical Research-Solid Earth, 106, 4247–4264, doi:
807   10.1029/2000JB900373, 2001.
808 Moraetis, D., Mouslopoulou, V., and Pratikakis, A.: Sorption of the Rare Earth Elements and
809   Yttrium (REE-Y) in calcite: the mechanism of a new effective tool in identifying
810   paleoearthquakes on carbonate faults. Geophysical Research Abstracts, 17, EGU2015-
811   3437, 2015.
812 Mouslopoulou, V., Moraetis, D., and Fassoulas, C.: Identifying past earthquakes on carbonate
813   faults: Advances and limitations of the 'Rare Earth Element' method based on analysis of
814   the Spili Fault, Crete, Greece. Earth and Planetary Science Letters, 309, 45–55, 2011.
815 Mozafari, N., Özkaymak, C., Sümer, Ö, Tikhomirov, D., Uzel, B., Yeşilyurt, S., Ivy-Ochs, S.,
816   Vockenhuber, C., Sözbilir, H., and Akçar, N.: Seismic history of western Anatolia during
817   the last 16 kyr determined by cosmogenic ^{36}Cl dating. Swiss Journal of Geosciences 115,
818   5, https://doi.org/10.1186/s00015-022-00408-x, 2022.
819 Muhs, D.R., Budahn, J., Avila, A., Skipp, G., Freeman, J., Patterson, D.: The role of African
820   dust in the formation of Quaternary soils on Mallorca, Spain and implications for the
821   genesis of Red Mediterranean soils. Quaternary Science Reviews 29, 2518–2543, 2010.
822 Muzikar, P., Elmore, D., and Granger, D.E.: Accelerator mass spectrometry in geologic
823   research. Geological Society of America Bulletin, 115, 643-654, doi: 10.1130/0016-
824   7606(2003)115, 2003.
825 Nuriel, P., Rosenbaum, G., Zhao, J.-X., Feng, Y., Golding, S.D., Villemant, B., and
826   Weinberger, R.: U-Th dating of striated fault planes. Geology, 40, 647–650, 2012.
827 Palumbo, L., Benedetti, L., Bourlès, D., Cinque, A., and Finkel, R.: Slip history of the
828   Magnola fault (Apennines, Central Italy) from ^{36}Cl surface exposure dating: evidence for
829   strong earthquakes over the Holocene. Earth and Planetary Science Letters, 225, 163–
830   176, doi: 10.1016/j.epsl.2004.06.012, 2004.
831 Papanikolaou, I.D., Roberts, G.P., Deligiannakis, G., Sakellariou, A., and Vassilakis, E.: The
832   Sparta Fault, Southern Greece: From segmentation and tectonic geomorphology to
833   seismic hazard mapping and time dependent probabilities. Tectonophysics, 597–598, 85–
834   105, 2013.
835 Pavlides, S. and Caputo, R.: Magnitude versus faults' surface parameters: quantitative
836   relationships from the Aegean Region. Tectonophysics, 380, 159–188, 2004.
837 Pope, R.J. and Wilkinson, K.N.: Reconciling the roles of climate and tectonics in Late
838   Quaternary fan development on the Spartan piedmont, Greece. In: A.M. Harvey, A.E.
839   Mather, and M. Stokes, (Eds), Alluvial Fans: Geomorphology, Sedimentology,
840   Dynamics. Geological Society, London, Special Publications, 251, 133–152. The
841   Geological Society of London, 2005.
842 Röshoff, K. and Cosgrove, J.: Sedimentary dykes in the Oskarshamn-Västervik area. A study
843   of the mechanism of formation. SKB Report R-02-37, 98 pp, 2002.
844 Roy, C.J.: Clastic dykes of the Pikes Peak region. Geological Society of America Bulletin,
845   57, 1226, 1946.
846 Sagy, A. and Brodsky, E.E.: Geometric and rheological asperities in an exposed fault zone.
847   Journal of Geophysical Research, 114, B02301, doi: 10.1029/2008JB005701, 2009.
848 Schlagenhauf, A., Gaudemer, Y., Benedetti, L., Manighetti, I., Palumbo, L.,
849   Schimmelpfennig, I., Finkel, R., and Pou, K.: Using in situ Chlorine-36 cosmonuclide to
850   recover past earthquake histories on limestone normal fault scarps: a reappraisal of
851   methodology and interpretations. Geophysical Journal International, 182, 36–72, doi:
852   10.1111/j.1365-246X.2010.04622.x, 2010.

853   Sharma, P., Kubik, P.W., Fehn, U., Gove, H.E., Nishiizumi, K. and Elmore, D.: Development
854   of Cl-36 Standards for AMS. Nuclear Instruments & Methods in Physics Research
855   Section B-Beam Interactions with Materials and Atoms, 52, 410-415, doi: 10.1016/0168-
856   583X(90)90447-3, 1990.
857   Sikora, F.J. and Moore, K.P. (Eds.): Soil Test Methods from the Southeastern United States.
858   Southern Cooperative Series Bulletin, 419, 211 p., 2014.
859   Stone, J.O.: Air pressure and cosmogenic isotope production. Journal of Geophysical
860   Research, 105, B10, 23753-23759, 2000.
861   Stone, J.O.: Terrestrial chlorine-36 production from spallation of iron. In: Abstract of 10th
862   International Conference on Accelerator Mass Spectrometry, Berkeley, California, USA.,
863   2005.
864   Stone, J.O., Allan, G.L., Fifield, L.K., and Cresswell, R.G.: Cosmogenic chlorine-36 from
865   calcium spallation. Geochimica et Cosmochimica Acta, 60, 679-692, doi: 10.1016/0016-
866   7037(95)00429-7, 1996.
867   Takahashi, Y., Chatellier, X., Hattori, K.H., Kato, K., and Fortin, D.: Adsorption of rare earth
868   elements onto bacterial cell walls and its implication for REE sorption onto natural
869   microbial mats. Chemical Geology, 219, 53–67, 2005.
870   Tesson, J., Pace, B., Benedetti, L., Visini, F., Delli Rocioli, M., Arnold, M., Aumaître, G.,
871   Bourlès, D.L., and Keddadouche, K.: Seismic slip history of the Pizzalto fault (central
872   Apennines, Italy) using in situ-produced ^{36}Cl cosmic ray exposure dating and rare earth
873   element concentrations. Journal of Geophysical Research Solid Earth, 121, 1983–2003,
874   doi:10.1002/2015JB012565, 2016.
875   Woodcock, N.H. and Mort, K.: Classification of fault breccias and related fault rocks.
876   Geological Magazine, 145, 435–440, doi: 10.1017/S0016756808004883, 2008.
877   Zreda, M. and Noller, J.: Ages of prehistoric earthquakes revealed by cosmogenic chlorine-36
878   in a bedrock fault scarp at Hebgen Lake. Science, 282, 1097–1099, 1998.

879   **Table 1:** Parameters used to give best fits of modelled profiles to measured ^{36}Cl
880   concentration profiles, following Schlagenhauf et al. (2010).

Profile	α (°)	β (°)	γ (°)	Scarp (cm)	ρ_{rock} (g cm^{-3})	$\rho_{colluvium}$ (g cm^{-3})	^{36}Cl P$_o$ (at. g^{-1} yr^{-1})	ε (mm yr^{-1})	Pre (yr)	Age (kyr B.P.)	Slip (cm)	RMSw	AICc	χ^2_{red}
Fig. 3a	42	61	20	730	2.65	1.95	59.4	0.02	10 300	5.98 ± 0.4, 3.8 ± 0.3, 3.2 ± 0.3, 2.8 ± 0.2, 2.3 ± 0.2	140, 120, 130, 120, 140	10	859	3
Fig. 3b	49	61	20	730	2.65	2.01	59.4	0.02	3 900	2.5 ± 0.2, 2.3 ± 0.2	60, 140	5	406	2
Fig. 3c	42	61	20	742	2.65	1.95	59.4	0.02	12 000	8.6 ± 0.6, 5.8 ± 0.4, 3.8 ± 0.3, 3.2 ± 0.3, 2.5 ± 0.3	140, 120, 130, 120, 140	19	1338	7
Fig. 3d	42	61	20	730	2.65	1.95	59.4	0.02	10 300	5.9 ± 0.4, 3.0 ± 0.3, 2.8 ± 0.2, 1.9 ± 0.2	240, 140, 180, 80	12	875	5

881   α is hanging wall colluvial surface dip angle; β is scarp dip angle; γ is the dip angle of the hillslope above the fault scarp; ε is
882   scarp erosion rate; Pre is pre-exposure; Age is inferred earthquake age(s) with 0 inserted to model scarp samples from below
883   the surface of the hanging wall colluvium; Slip is the inferred displacement for each earthquake. On each profile, the oldest age
884   and associated displacement, shown in grey, are fitted to the top of the vertical sample transect rather than fitted to a step in
885   ^{36}Cl concentration; RMSw is weighted root mean square; AICc is Akaike Information Criterion; χ^2_{red} is reduced Chi-square.
886   Model best fits for each data set are shown in black. The ^{36}Cl production rate of 59.4 ± 4.3 at g^{-1} yr^{-1} is taken from Lifton et al.
887   (2005).
888

889 **Figures**
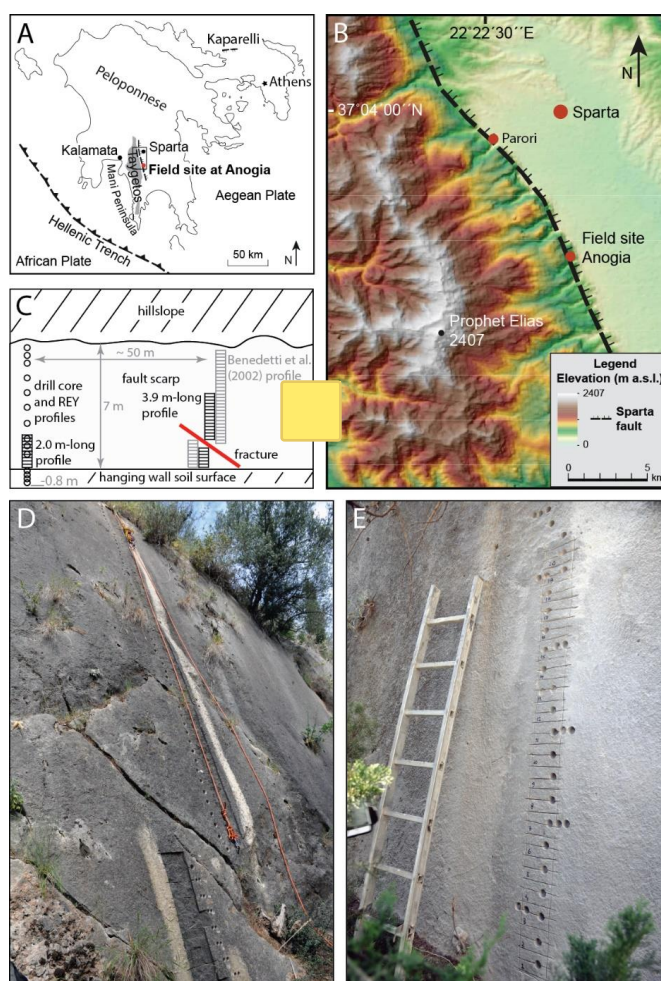
890

891 **Fig. 1:** Study site. A. The study site location in Peloponnese, Greece. Key tectonic features
892 are shown. Box indicates location of panel B. B. The location of the Sparta fault, separating
893 the Taygetos Mountains from the Sparta basin. The location of the Anogia field site used both
894 in this study and in Benedetti et al. (2002) is shown. Benedetti et al. (2002) located a second
895 sampling transect at Parori (also shown). The digital elevation model has a 24 m resolution
896 and is derived from ASTER GDEM (GDEM2), which is a product of NASA and METI
897 (Japan). C. Schematic diagram of the Sparta fault scarp at Anogia, showing the locations of
898 our vertical ^{36}Cl and REY sampling transects, and the ^{36}Cl sampling transect of Benedetti et
899 al. (2002). D. Photograph showing the location of our 3.9 m-long profile, prior to sampling.
900 The existing sample scar is from Benedetti et al. (2002). E. Photograph showing the location
901 of our REY and drill core profiles, after sampling, and our 2.0 m long profile, before
902 sampling.
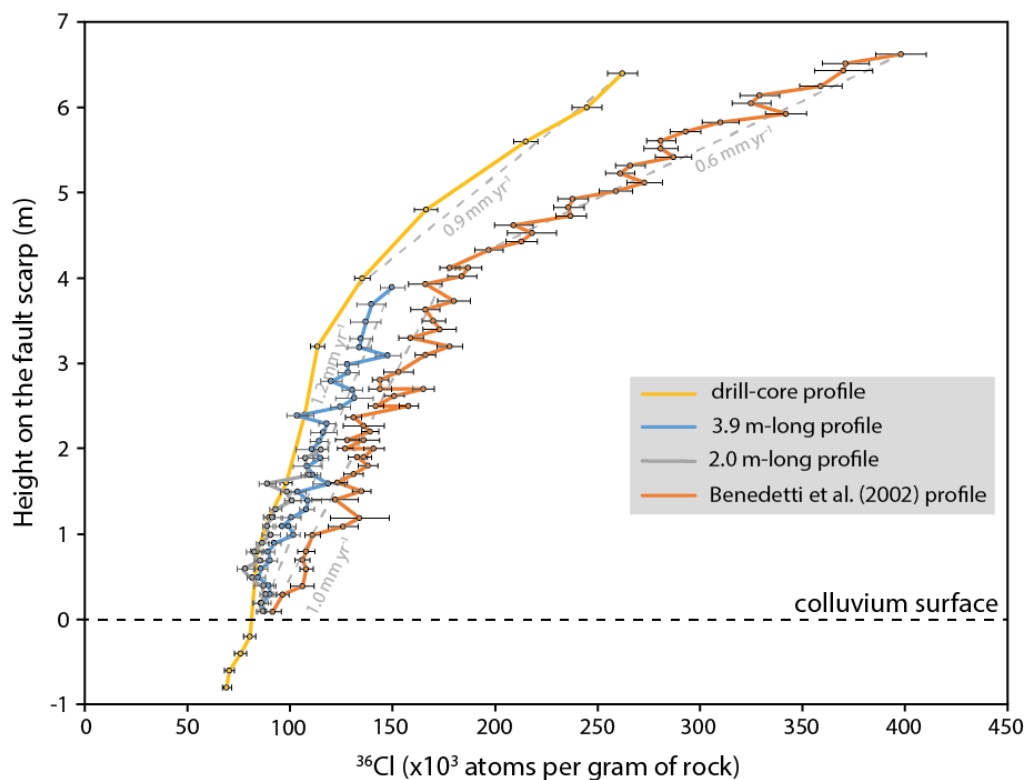
Fig. 2: Sparta fault ^{36}Cl concentration profiles. Error bars indicate 1σ measurement uncertainties. Time-averaged uplift rates inferred from profile gradients are shown in grey. For the lower, more recently exposed, parts of the scarp surface, uplift rates are calculated for time starting from the present day. If uplift rates are alternatively calculated as occurring prior to the subaerial exposure of the lowermost samples by the most recent earthquake, cumulative uplift rates increase to 2.8 mm yr^{-1} and 1.8 mm yr^{-1} for the lower parts of the 3.9 m-long and Benedetti et al. (2002) profiles, respectively.
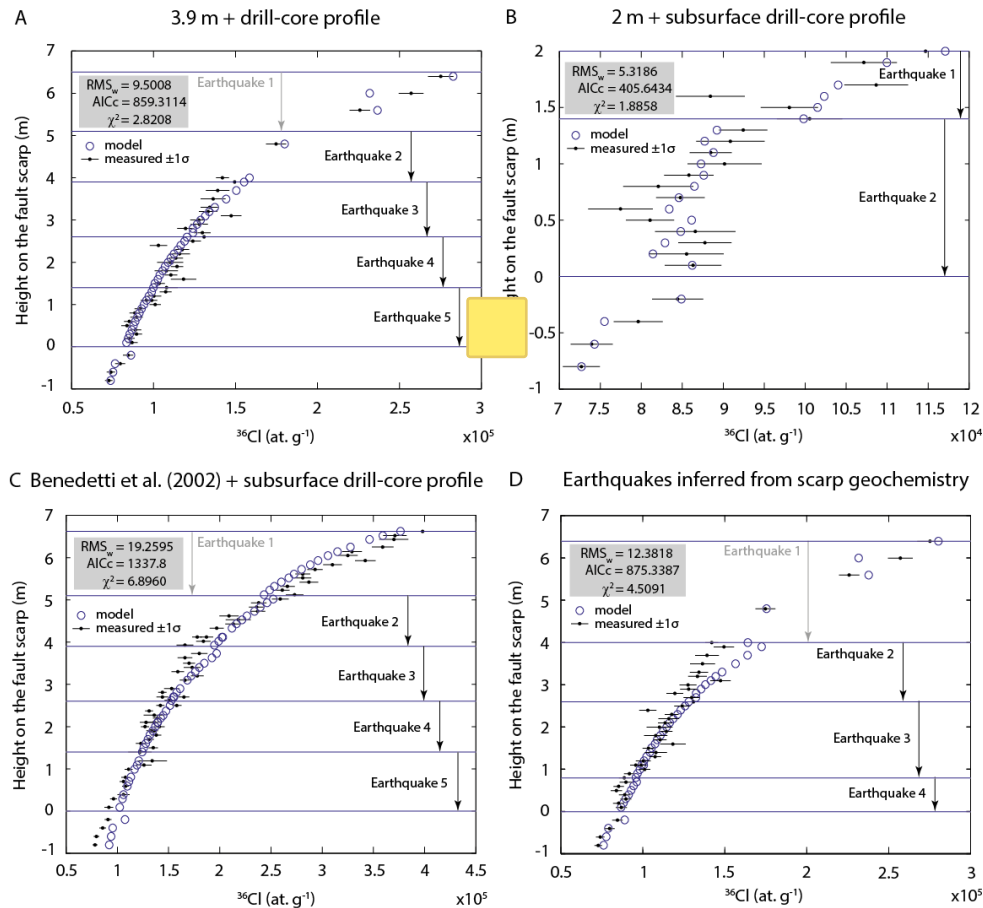
Fig. 3: Best fits of profiles modelled according to Schlagenhauf et al. (2010) to measured
Sparta fault ^{36}Cl concentration profiles. Down-arrows indicate the section of scarp exhumed
during each earthquake. Best fits of modelled profiles to measured data are indicated by
lowest attainable values for each of RMS$_w$, χ^2_{red}, and AICc. A. Anogia 3.9 m profile plus drill
core profile data above 3.9 m and below the present hanging wall colluvium surface. B.
Anogia 2.0 m profile plus drill core profile data from below the present hanging wall
colluvium surface. C. Benedetti et al. (2002) data, remodeled using the same parameters as
for panel A . The modelled profile is smooth because scarp composition is based on a mean
value taken from our data. Our drill core subsurface samples were also used to help remodel
the Benedetti et al. (2002) data, which required adding 13% on to their measured
concentrations. D. Same profile as in A but with earthquakes inferred from the fault scarp
geochemistry.
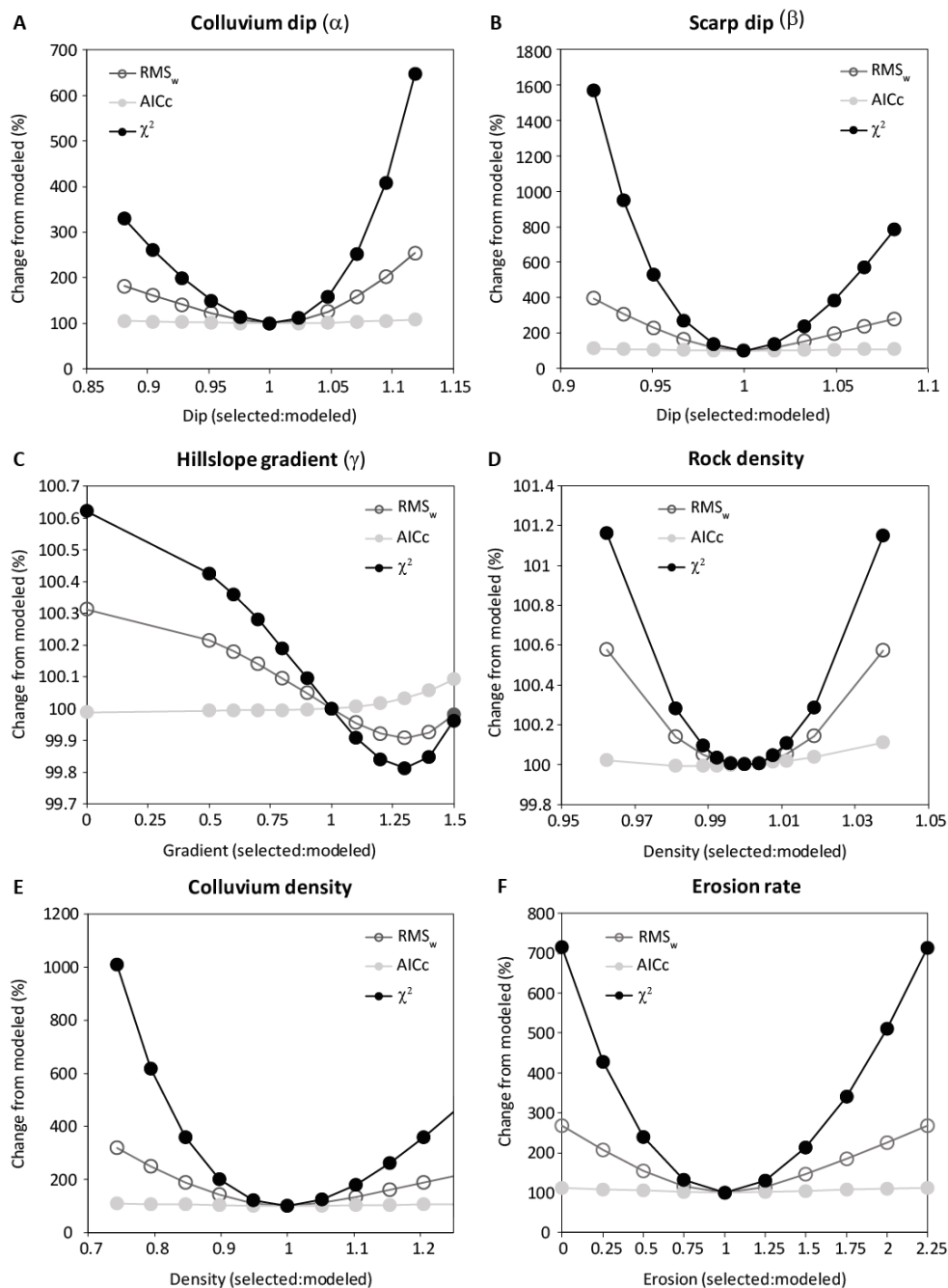
Fig. 4: Sensitivity of fits of profiles modelled according to Schlagenhauf et al. (2010) to measured Sparta fault [36]Cl concentration profiles, according to input parameters. A. Colluvial wedge dip B. Scarp dip C. Slope angle above the scarp. D. Scarp rock density E. Colluvium density F. Scarp erosion rate.
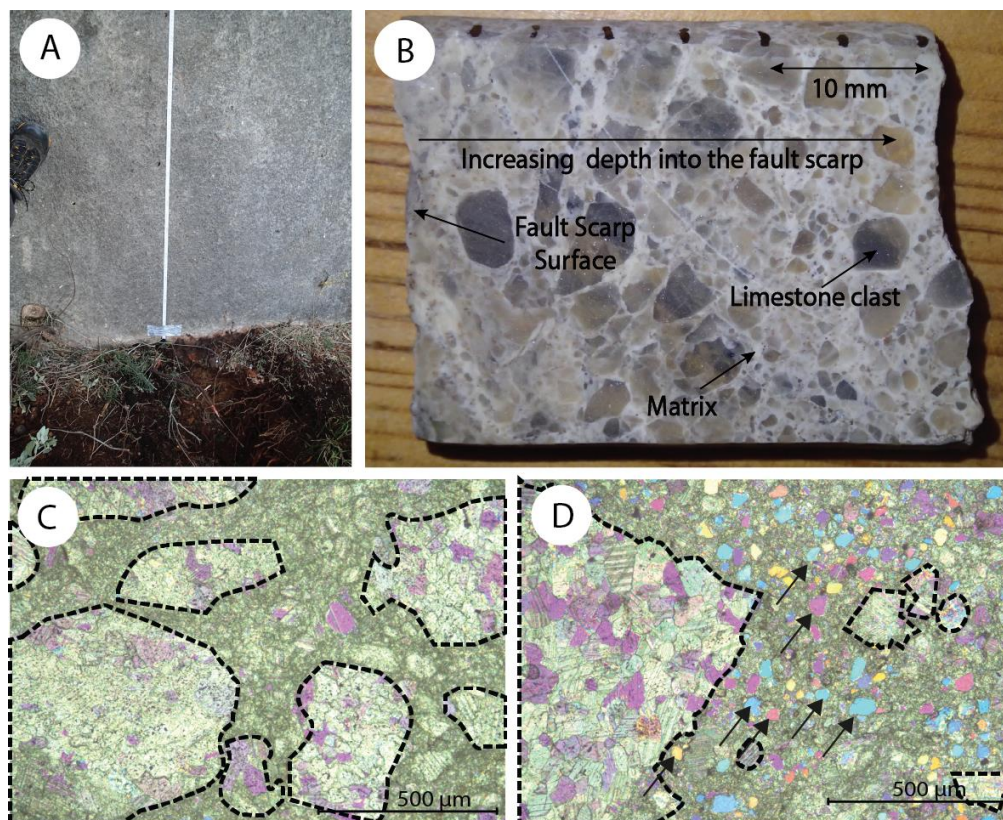
933
934 **Fig. 5:** The heterogeneous fault breccia that comprises the Sparta fault scarp surface. A. The
935 Sparta fault scarp surface appears smooth and homogenous, as illustrated by this photograph
936 of the scarp base at Anogia (upper half of the dug trench in the foreground). B. Fault breccia
937 is revealed in a cut drill core, where clasts of host limestone are cemented in a fine matrix. C.
938 A photomicrograph shows limestone clasts (dotted outlines) comprising about 60% of the
939 thin section area. D. A photomicrograph shows fine matrix comprising about 60% of the thin
940 section area. Arrows indicate quartz.
941

942
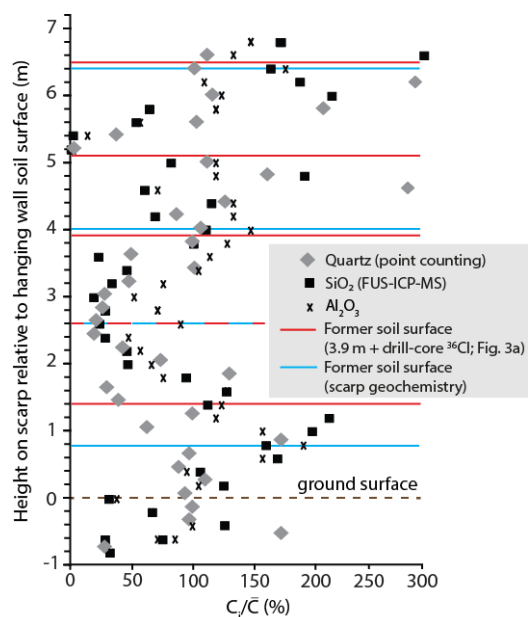
Fig. 6: Concentrations of Al_2O_3 and SiO_2, and quartz abundances from point counting, along
a vertical profile, Sparta fault scarp, Anogia. The concentration of each element (C_i) is
normalized to its mean concentration through the profile ($C_i / \bar{C}$). The locations of former soil
surface horizons inferred from [36]Cl concentrations and from the scarp geochemistry are
shown for reference.
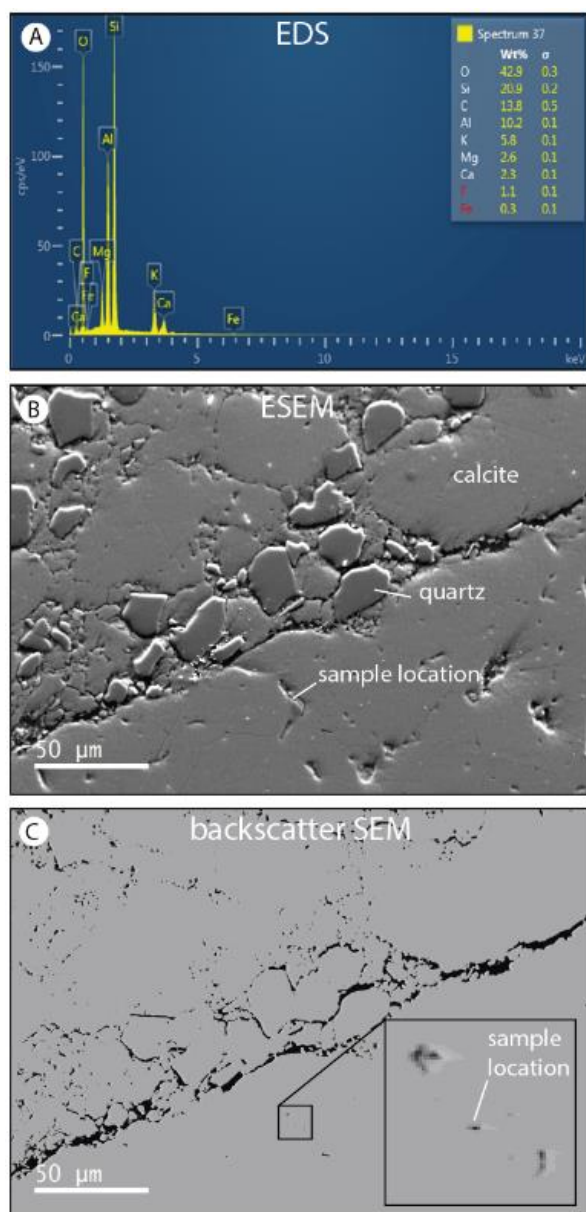
948
949 **Fig. 7:** Energy-dispersive X-ray spectroscope (EDS) elemental abundances, and
950 environmental scanning electron microscope (ESEM) and backscatter SEM imagery of a thin
951 section of fault breccia comprising the Sparta fault scarp surface at 1.1 m above the hanging
952 wall. (A). Element abundances in a pore, the location of which is shown in panels B and C.
953 Si, Al, and K are abundant relative to Ca, which indicates that clay, e.g., illite, is lining the
954 pore. (B) Quartz is an abundant constituent of the thin section matrix. (C) Porosity, shown in
955 black; note its spatial association with quartz. The location of the sample used in panel A is in
956 a small pore, shown in the inset.
957
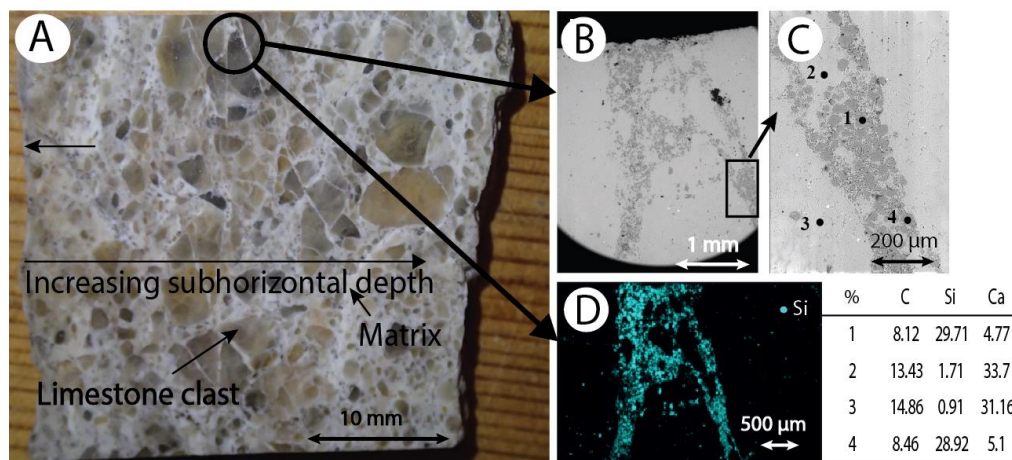
Fig. 8: Concentrations of Si in the Sparta fault breccia, 1.1 m above the scarp base at Anogia.
A. A cut drill core from the Sparta fault scarp at Anogia showing limestone clasts cemented
in fine matrix. The circled fine matrix is examined under high resolution in panels B to D. B.
An ESEM image showing the sample location for spot elemental analysis (rectangle). C.
Sample points for elemental analysis using EDS, with values shown in the table. D. The
abundance of Si in the fine matrix illustrated in magenta for the circled part of the thin
section shown in panel A.
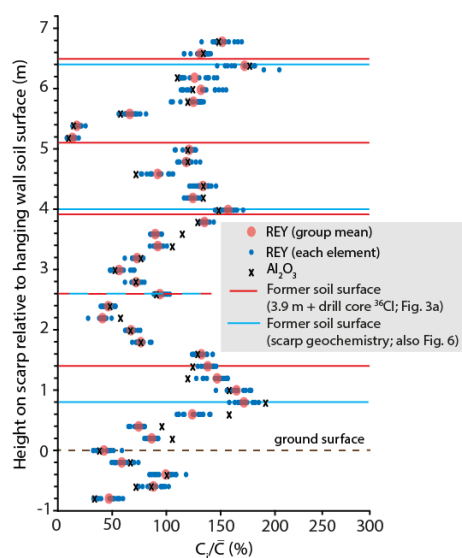
Fig. 9: Concentrations of rare-earth elements and yttrium (REY) along a vertical profile on
the Sparta fault at Anogia. Mean values for all REY elements at each sample point are shown
in red dots, whereas individual REY elements are shown in blue dots. The concentration of
each element (C_i) is normalized to its mean concentration through the profile ($C_i /\overline{C}$).

972 Concentrations of Al$_2$O$_3$ and former soil surface horizons inferred from [36]Cl concentrations
973 profiles and geochemical data, are shown for reference.
974
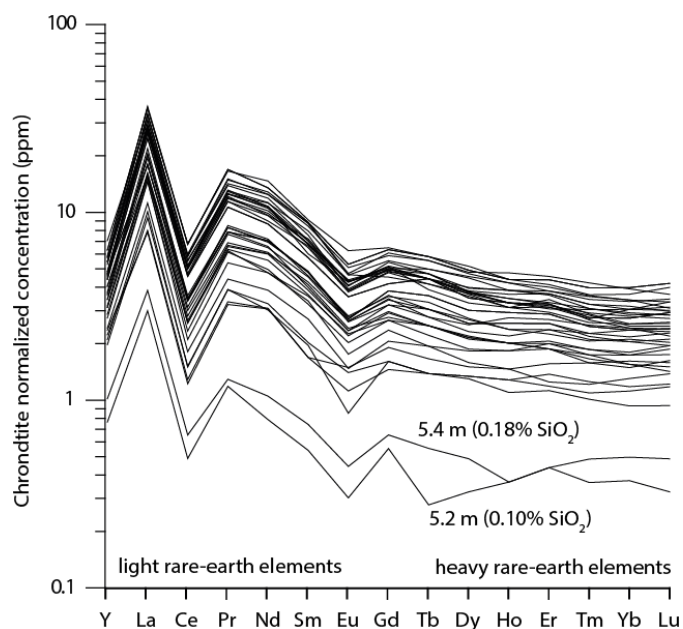
975
976 **Fig. 10:** Concentrations of rare-earth elements and yttrium (REY) normalized to chondrite
977 composition (McDonough and Sun, 1995) for the Sparta Fault scarp at Anogia. Each line
978 shows a measured location on the scarp surface. The two low REY outliers at 5.2 m and 5.4
979 m also have exceptionally low SiO$_2$.
980
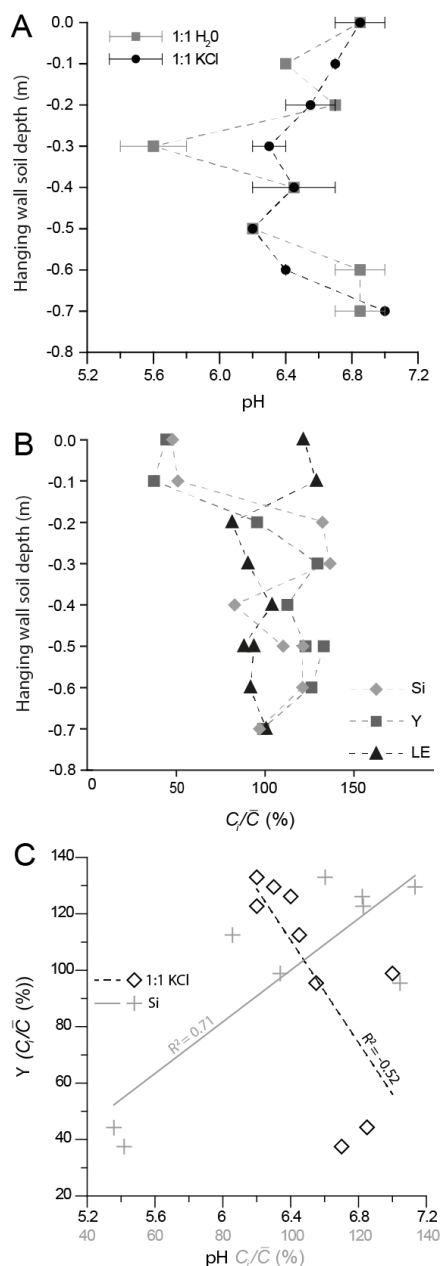
Fig. 11: Hanging wall soil chemistry, adjacent to the Sparta fault scarp at Anogia. A. Soil pH along a vertical profile measured from soil mixed with distilled H_2O and 1M KCl. Uncertainty ranges show the ≤ 0.5 resolution of the indicator strips. B. Concentrations of Si, Y, and elements too light to be measured using handheld XRF (LE, including C) along the vertical soil profile. Each element has been normalized through division by its mean concentration through the soil. C. Y concentrations plotted against pH (measured from 1:1 KCl) and Si concentration at each measured depth interval beneath the soil surface.